Techno-Economic Analysis of Candidate Oxide Materials for Thermochemical Storage in Concentrating Solar Power Systems

Reiner Buck[1]*, Christos Agrafiotis[2], Stefania Tescari[2], Nicole Neumann[2] and Martin Schmücker[3]

[1]German Aerospace Center (DLR), Institute of Solar Research, Stuttgart, Germany, [2]German Aerospace Center (DLR), Institute of Future Fuels, Köln, Germany, [3]HRW University of Applied Sciences, Mülheim/Ruhr, Germany

The thermal storage capability is an important asset of state-of-the-art concentrating solar power plants. The use of thermochemical materials, such as redox oxides, for hybrid sensible/thermochemical storage in solar power plants offers the potential for higher specific volume and mass storage capacity and as a consequence reduced levelized cost of electricity making such plants more competitive. For the techno-economic system analysis, three candidate redox materials were analyzed for their cost reduction potential: cobalt-based, manganese–iron–based, and perovskite-based oxide materials. As a reference process the use of inert commercial bauxite particles (sensible-only storage) was considered. A solar thermal power plant with a nominal power of 125 MW$_e$ and a storage capacity of 12 h was assumed for the analysis. For each storage material a plant layout was made, taking the specific thermophysical properties of the material into account. Based on this layout a particle break-even cost for the specific material was determined, at which levelized cost of electricity parity is achieved with the reference system. Cost factors mainly influenced by the material selection are storage cost and steam generator cost. The particle transport system cost has only a minor impact. The results show differences in the characteristics of the materials, for example, regarding the impact on storage size and cost and the steam generator cost. Regarding the economic potential of the candidate redox materials, the perovskite-based particles promise to have advantages, as they might be produced from inexpensive raw materials.

Keywords: solar power, thermochemical energy storage, particles, redox reaction, techno-economic optimization

INTRODUCTION

The use of thermochemical energy storage (TCS) materials, such as redox pair oxides, for hybrid sensible/thermochemical storage in concentrated solar power (CSP) plants (Wong, 2011) can potentially reduce the levelized cost of electricity (LCOE) and make such plants more competitive. The basic operation concept is that a large part of the heat supplied from solar concentration facilities to a solar receiver is employed to drive the endothermic reduction of the oxidized state of an oxide (the one with the higher valence of the cation metal) to the reduced one. The heat stored in the reduced oxide can be recovered at will, as the enthalpy of the reverse exothermic oxidation reaction, and used for electricity generation during off-sun operation. In

contrast to other TCS schemes (e.g., carbonation/decarbonation or hydration/dehydration), both reactions can be performed in principle under direct contact of the oxide with air, waived thus of the need for an additional heat exchanger as well as of handling other-than-air gases like carbon dioxide or steam. The same feature renders them compatible with the quest for development of higher efficiency CSP plants operating via air-Brayton gas turbine power cycles instead of the currently employed Rankine steam one, since the input in a gas turbine is an air stream of high pressure and temperature (Schrader et al., 2015). This high-temperature air stream could be achieved by exploiting the enthalpy of sufficiently exothermic air-oxide oxidation reactions between air and the oxide instead of utilizing a gas combustor burning fossil fuels.

The ideas for eventual implementation of these redox oxide–based TCS concepts in commercial, utility-scale CSP plants capitalize on approaches for sensible-only high-temperature storage in ceramic media (Khare et al., 2013) already industrially practiced or currently under consideration and investigation. In this context, the concepts proposed so far for the integration of such systems in CSP plants can be categorized in two broad concepts depending on whether the solid oxide, in addition to its role as the storage medium, is also employed as the solar energy harvesting medium and consequently as the heat transfer fluid (HTF) or not.

The first concept utilizes moving particle streams as a combined HTF/storage medium, which stems from recent approaches considering inexpensive, chemically inert, refractory ceramic particles as alternative heat transfer and extremely high temperature storage (T > 1,000°C) media for CSP plants (Siegel et al., 2015). Oxide particle streams in their oxidized state are transported to the top of a solar tower where they are thermally reduced in a solar particle receiver. This receiver can be, for example, a rotary kiln (Neises et al., 2012), a fluidized or spouted bed type (Flamant et al., 2013; Ma et al., 2014), a gravity-led inclined "sliding-bed" type (Schrader et al., 2020), or a centrifugal receiver recently introduced and developed by DLR (Wu et al., 2014). The reduced particles are stored in a hot particle storage tank and subsequently fed to an oxidation reactor for power generation when and where needed. At the end of this step they are oxidized, stored in a cold particle storage tank, and then recirculated back to the solar receiver for a new cycle.

Alternatively, in a second approach, a different heat transfer fluid—and in the particular case of oxides, air is the obvious choice—heated in the solar receiver can indirectly heat a non-moving oxide storage medium in the form of either particle bed or monolithic structures like honeycombs/bricks reducing it during on-sun operation. During off-sun operation "cold" air is introduced and flows through the volume of the solid storage medium, oxidizes it, and consequently is heated by the oxidation reaction enthalpy to the levels required for its introduction to the power block. Again, this approach stems from commercial high temperature regenerative storage systems, for example, the so-called Cowper stove used with blast furnaces that consist of a stacked firebrick storage medium (Tamme et al., 1991) as well as with similar sensible heat storage units employed in air-operated solar thermal power plants, like the one of DLR at Jülich, Germany (Zunft et al., 2014).

Both approaches essentially target to convert a chemically inert, sensible-only storage ceramic medium (particle, granule, honeycomb, or brick) to a hybrid sensible/TCS one by introducing chemical reaction functionality (with oxygen) in it in the same volume. Hence, such hybrid sensible/TC systems using oxide-gas reactions have the potential of greatly shrinking the size of storage subsystems/tanks. This becomes especially relevant for longer storage durations, where the combination of CSP and thermal storage may be most competitive with regards to LCOE, for example, in comparison to PV and battery storage (Schöniger et al., 2021).

DLR is investigating both approaches in conjunction with issues on the material composition itself. On the materials' side, potential candidate of redox pair oxides that can be thermally reduced in the temperature range of interest without requiring very low oxygen partial pressures, that is, in direct contact with atmospheric air includes BaO_2/BaO, Co_3O_4/CoO, Mn_2O_3/Mn_3O_4, CuO/Cu_2O, and Fe_2O_3/Fe_3O_4 (Wong, 2011) as well as their mixed compositions (Block and Schmücker, 2016). Among them, extensive work has been performed on the Co_3O_4/CoO system due to its very high energy density (ΔH of the reaction in kJ/kg of solid oxide), stoichiometric and fully reversible reaction, and excellent long-term cyclic stable performance. Thus, along the second approach above pursued in project RESTRUCTURE, the concept evolved to a 74 kWh$_{th}$ hybrid sensible-TCS unit encompassing 88 kg of Co_3O_4 coated on cordierite honeycombs that has clearly manifested recordable substantial temperature effects due to chemical reactions and is the largest oxide TCS system developed and experimentally validated so far (Tescari et al., 2017). However, cobalt is mined in areas of the world generally acknowledged for mismanagement, environmental degradation, and adverse impacts to public health and therefore on the way to a low-carbon economy and ethical and societal issues advocate for its eventual elimination from such energy-related technologies (including electric energy storage in batteries). Thus, research is focused on alternative systems based on inexpensive, non-critical, abundant, and environmentally safe materials such as Ca⁻, Mn⁻, and Fe⁻ based redox oxides, despite their lower energy storage density compared to Co_3O_4.

In the RedoxStorE project a CSP system utilizing particles as HTF and storage material is investigated. In this context particle-based options for such a system were analyzed and the relevant components were further developed. Experimental work focused on the development of suitable particles (Wokon et al., 2017a; Wokon et al., 2017b; Preisner et al., 2018), high temperature particle receivers for the thermal reduction of these particles (Tescari et al., 2020), and a particles-to-air heat exchanger for thermochemical oxidation of the reduced particles and heat recovery (Preisner and Linder, 2020). According to the rationale above, manganese–iron–based redox particles were investigated experimentally in detail, as an example of earth-abundant, environmental-friendly, and inexpensive thermochemical particles (Wokon et al., 2017a; Wokon et al., 2017b). In parallel, such kinds of solar particle receivers based on perovskites have been proposed in the United States, within the so-called PROMOTES project (Miller et al., 2016). This concept
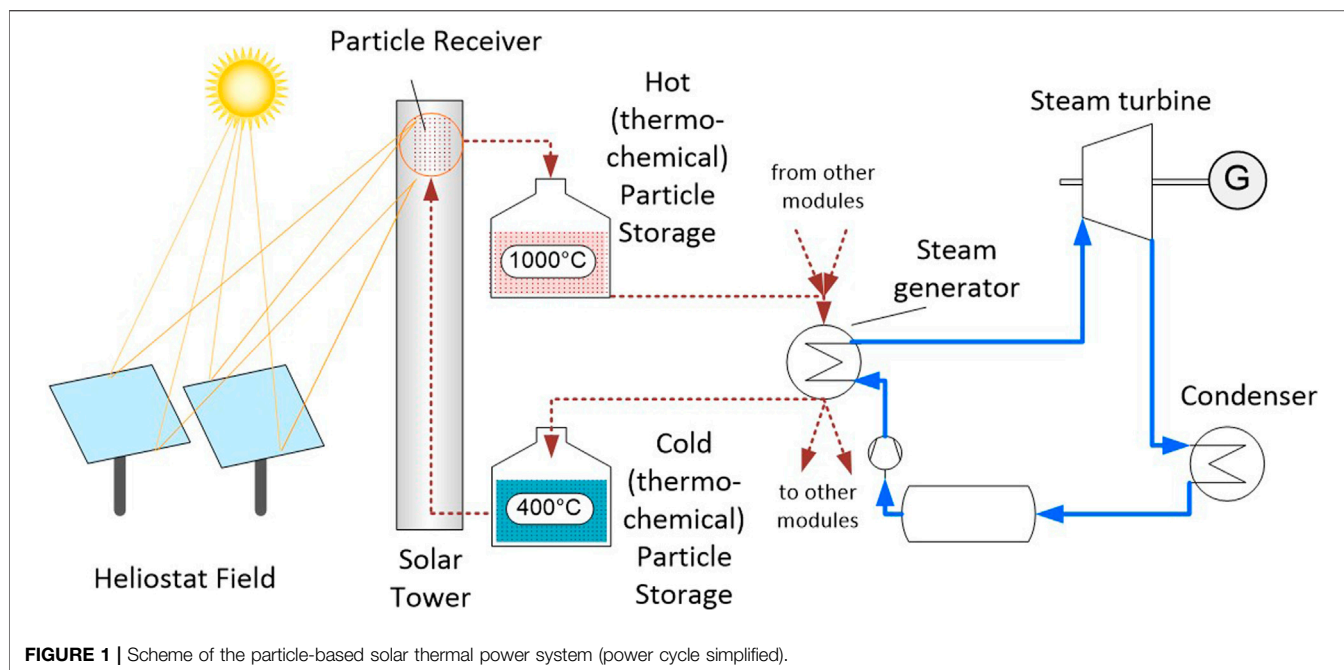
FIGURE 1 | Scheme of the particle-based solar thermal power system (power cycle simplified).

foresees a controlled atmosphere solar receiver chamber where the oxides at their oxidized state are thermally reduced under low oxygen partial pressure (slight or higher vacuum or under inert gas flow) and a reoxidation reactor, wherein the reduced particles react with pressurized air on-demand (Babiniec et al., 2016) in the context of coupling the process to an air-Brayton gas turbine cycle, as already discussed. In the latter design, the air is preheated by the compression stage, with no further preheating from other sources.

In parallel to more fundamental materials–composition screening studies and demonstration of effective reactor/heat exchanger concepts, there is a need to illustrate how the various components can be materialized in storage modules effectively incorporated in the operation of a full CSP plant. The large-scale adoption of oxide-based TCS in such real CSP plants will depend on the one hand on whether such materials can be produced cost-effectively at large-scale, but, most crucially, on whether such concepts can eventually compete with current industrial scale sensible–only storage ones, generally implemented with inexpensive systems, to justify the introduced plant complexity. Hence, the present work is targeted to such a comparative techno-economic system analysis, considering three candidate redox materials for their cost reduction potential: cobalt-based, manganese-based, and perovskite-based oxide materials. As a reference process, the use of inert commercial bauxite particles as sensible-only storage medium was considered. The paper presents the results of this techno-economic analysis.

A first assessment of the same or similar materials was performed in a study by Buck et al., (2020) using simplified cost assumptions. In this study, new compositions for the manganese-based and perovskite material are assessed. In addition, further refinement on some cost assumptions like the

ground transportation cost was introduced. The cost for heliostats and bauxite particles was also revised to be in accordance with the US-DoE next generation CSP "Gen3" (Mehos et al., 2017) system analysis assumptions.

SYSTEM DESCRIPTION

The study investigates a solar power plant with different storage materials. The concentrating solar power (CSP) plant has a nominal power of $125\,MW_e$ and includes thermal storage with a capacity of 12 h. The solar subsystem consists of a multi-tower configuration with 14 identical solar tower modules, feeding hot particles to a common high-efficiency steam cycle for power production. **Figure 1** shows a scheme of the system under consideration.

An advanced subcritical steam power cycle with reheat and multiple preheating stages is assumed, as described in (Buck and Giuliano, 2019). In the steam generator, high pressure steam is heated from 261 to 620°C; in the reheat section, the intermediate pressure steam is reheated from 426 to 620°C. For this steam process, a net cycle efficiency of 43% is calculated. Using this efficiency, a thermal input power of $291\,MW_{th}$ is required from the solar subsystem for nominal load operation. For the layout and costing study the steam generator is considered as a single heat exchanger, that is, the primary (high pressure) heater and the (intermediate pressure) reheater are not considered separately.

The multi-tower concept is selected since the considered receiver technology, the centrifugal particle receiver CentRec® developed by DLR (Ebert et al., 2016; Ebert et al., 2018), has inherent size limitations due to its rotating drum design. As of now, a receiver limit of $50\,MW_{th}$ per receiver is assumed. This size corresponds to an outer drum diameter of about 7.5 m and an

aperture diameter of about 5.4 m, a size which seems to be feasible based on knowledge about existing industrial rotary kiln and milling units. In total 14 solar tower modules are assumed, with each of the modules consisting of a receiver with a design point (DP) power of 50 MW$_{th}$, a tower, a heliostat field, and a thermal storage composed of two storage containments integrated into the tower structure (hot storage above cold storage). The total thermal system power of all modules is 700 MW$_{th}$ at DP conditions. With the power cycle demand of 291 MW$_{th}$ this represents a solar multiple of 2.4.

The upper particle temperature in the process is assumed as 1,000°C. This represents the temperatures of the receiver exit, the hot particle storage, and the steam generator particle inlet. For the lower temperature, representing steam generator particle outlet, cold particle storage, and receiver inlet conditions, a value of 400°C is set. This temperature range includes the reduction temperatures of all three thermochemical oxides under study. The comparison implies that the same open-air centrifugal receiver will be employed for the thermal reduction of the thermochemical oxide particles, and therefore this reduction will take place under air atmosphere. Just like the chemically inert particles, the thermochemical ones are stored in a hot and a cold storage bin after their reduction and oxidation, respectively. The thermochemical characteristics of the particles were considered by approximated total enthalpy values at the high and low operation temperature points in the cycle.

PERFORMANCE AND COST ASSUMPTIONS

The layout of the solar subsystem (heliostat field, tower, and receiver) is not affected by the material selection for the thermochemical particles, meaning fix cost for these components. Cost factors influenced by material selection are the storage cost, the steam generator cost, and the particle transport system cost. System performance is hardly affected by the material selection, only the effect of changed particle mass flow has a small impact on annual energy yield, due to changes in parasitic power. Based on the total system cost and annual electricity generation, the LCOE is calculated. All cost data is given in Euro (€).

Performance and cost assumptions are selected in many aspects similar to the assumptions given in the Gen3 road map (Mehos et al., 2017) and related documents.

Plant Site

For the present analysis, a site near Daggett (California, United States) is considered. The site is located at a latitude of 34.85°north and a longitude of 116.79°west. The altitude of the site is 588 m above sea level. The annual direct normal irradiance (DNI) is reported as 2,791.4 kWh/m^{2}a.

Steam Power Cycle

As a steam power cycle a high efficiency power block with 620°C/125 bar live steam conditions is assumed (Buck and Giuliano, 2019). The power block is rated at 125 MW$_e$ with a

net efficiency of 43%. For the cost analysis, the power cycle and the steam generator are treated as separate items, since the cost of the latter is influenced by the operating temperature conditions while the power cycle cost is not. For the cost of the power cycle without steam generator a fixed specific cost of $C_{sp,pc}$ = 700 €/kW$_e$ is assumed. This results in a power cycle cost C_{pc} of 87.5 Mio €.

Steam Generator

The operating conditions in the steam generator change when thermochemical particles are used, compared to the situation with sensible-only heating. When chemically active particles are used the reaction keeps the temperature level higher in the steam generator, while transferring the chemically stored heat.

A moving bed particle heat exchanger is foreseen for the steam generator of the power cycle. In this heat exchanger type, the solid particles are moving slowly across the heat exchanger tubes, driven by gravity [6]. The mass flow is controlled by variable gate valves at the cold exit of the heat exchanger. The required heat transfer area of this heat exchanger is calculated as follows:

$$A_{HX,0} = \frac{P_{el}/\eta_{pc}}{h_{SG} \cdot \Delta T_{log}}. \tag{1}$$

In a study by Baumann and Zunft (2014), convective heat transfer coefficients up to 240 W/m^{2}K were measured for a tube bundle type heat exchanger with particle inlet temperatures ranging from 355 to 470°C. Since the particle heat exchanger for the steam power cycle is operated at much higher temperatures, radiative heat transfer will improve the overall heat transfer significantly. Therefore, a constant heat transfer coefficient h_{SG} of 300 W/m^{2}K is assumed. The mean logarithmic temperature difference ΔT_{log} for a heat exchanger in countercurrent flow configuration is calculated based on the solid particle temperature selection and the power cycle temperature levels. The water/steam temperatures in the steam generator are 261°C for the preheated water inlet and 620°C for the steam outlet.

The steam generator material temperatures are mainly defined by the steam conditions, as the highest heat transfer resistance will be between particles and tube material, that is, the tube material temperatures will be relatively close to the steam temperatures and quite independent of particle temperatures. Thus, the heat exchanger cost is assumed to be only a function of the required heat transfer area.

For thermochemical storage materials typically a higher temperature level is maintained in the steam generator, driven by the oxidation reaction that occurs while the material passes through the steam generator. Therefore, a higher driving temperature difference occurs in the heat exchanger regions where the reaction occurs. This effect is considered in the analysis by modifying the initially calculated heat exchanger area as follows:

$$A_{HX} = \frac{A_{HX,0}}{R_{tc}}. \tag{2}$$

The ratio R_{tc} is calculated from the particle specific heat capacity and the reaction enthalpy ΔH, as follows:

$$R_{tc} = \frac{\left(c_{p,part} \cdot \Delta T + \Delta H\right)}{c_{p,part} \cdot \Delta T}. \qquad (3)$$

Results for R_{tc} are given in "Results and Discussion." This simplified approach is taken since the characteristics of a heat exchanger for chemically active heat transfer materials is quite complex. In reality, factors like reaction kinetics and air stream requirements (blower, recuperator, and additional heat losses) limit the benefit of the redox reactions on heat transfer. The above reduction of the required heat exchanger area is considered quite positive for the thermochemical systems. A more realistic representation for the heat exchanger performance needs a detailed understanding and modeling of the heat exchanger and the reaction characteristics of the particles while passing through the heat exchanger. This is beyond the scope of the current study.

For the cost of the steam generator a correlation was derived using the MATCHE data base [Matches Equipment Cost, 2018] assuming Inconel 625 as tube material. With a correction factor, the high pressure of the steam system, a translation from 2014 cost into actual cost, and after converting from $ to € this resulted in the following correlation (Buck et al., 2020):

$$C_{HX} = 128122 \cdot A_{HX}^{0.66}. \qquad (4)$$

Heliostat Field

The heliostat field is composed of a large number of heliostats. Each heliostat is tracked in two axes and has a rectangular shape with 12.84 m width and 9.45 m height, covered with 4×7 facets of 3.21 m width and 1.35 m height. This results in a net reflective area of 121.34 m^2. A total beam error of 3.8 mrad is used for the Gaussian approximation of the beam reflected from the mirrors (as used in the HFLCAL optimization), representing the sunshape and a combined heliostat slope and tracking error of about 1.4 mrad. An effective reflectivity of 88% is assumed, accounting for the mirror reflectivity and an average dirt coverage of the mirrors. A specific cost $C_{sp,f}$ of 71 €/m^2 installed heliostat field is used, as prescribed by the Gen3 cost assumptions, taking the heliostat cost and the land preparation cost into account (Gonzalez-Portillo et al., 2021).

Tower

A tower is required to locate the solar receiver at a suitable height above the heliostat field. The tower height H_t is dominated by the heliostat field and receiver configuration, and is optimized together with other parameters. The cost of the tower is assumed (Weinrebe et al., 2014) as follows:

$$C_t = 1767767 \cdot e^{6.931E-3 \cdot H_t}. \qquad (5)$$

The tower includes the two integrated storage tanks, the tower wall structure serves also as the outer wall of the tanks.

Particle Receiver

The receiver technology for the multi-tower concept is based on the centrifugal particle receiver technology CentRec® (Ebert et al.,

2016), currently under development at DLR. The receiver uses the direct absorption principle, meaning that the dark particles are irradiated directly by the concentrated solar radiation and get heated from the absorbed radiation. A first demonstration receiver with about 2.5 MW_{th} peak power was installed at the DLR solar tower test facility in Jülich, Germany. Nearly 70 h of solar testing was carried out so far, and average particle outlet temperatures up to 965°C were achieved (Ebert et al., 2018). The receiver considered in this study has a circular aperture facing north at a certain tilt angle. The area A_{ap} of the circular aperture and the tilt angle are determined during the solar system optimization. A simplified receiver model is considered, with the absorbed power $P_{r,abs}$ defined as a function of intercepted power $P_{r,int}$ and receiver exit temperature $T_{r,ex}$ by following equation:

$$P_{r,abs} = \alpha \cdot P_{r,int} - \varepsilon\sigma\, A_{ap}\, T_{r,ex}^4 - h\, A_{ap}\, \left(T_{r,ex} - T_{amb}\right). \qquad (6)$$

For the CentRec® receiver, the effective values are set: solar absorptivity $\alpha = 0.95$, emissivity $\varepsilon = 0.9$, and convective heat transfer coefficient $h = 30$ W/m^2K. Ambient temperature T_{amb} is set to 300 K (27°C). These parameters were found to be a good fit to more detailed simulation results from finite element models.

Important to note is that the receiver has an open aperture, that is, the particle heating takes place at ambient air conditions. This is relevant for the perovskite material where the reaction enthalpy is strongly dependent on oxygen partial pressure.

Particle Transport System

The multi-tower system needs particle transportation in two ways: lifting the 400°C particles up to the receiver inlet ("vertical" particle transport) and transporting the particles between the solar tower modules and the central power station ("ground" particle transport).

When sufficient solar power is available for the receiver, the 400°C particles are lifted up to the receiver for heating. The heated particles are then flowing by gravitation to the hot storage. When the power block is operated, particles are charged from the hot storage into insulated transportation containers and then transported to the central unit. After being cooled down in the steam generator of the central power block, the colder particles are transported back in insulated containers to the solar tower modules and are either lifted up to the receiver (when enough solar power is available) or lifted to the inlet of the cold storage container. When more solar power is available than the power cycle actually uses, the hot storage fills up while the cold storage is emptied.

Vertical Particle Transport

A mine hoist system is foreseen for the vertical particle transport. Repole and Jeter (2016) have made a conceptual design for a hoist for a solar demonstration system with a thermal capacity of 60 MW_{th}. Since the selected solar tower module size is close to this capacity, this mine hoist design was taken as base value for the calculation of the cost for the specific configuration. Scaling factors are applied for conditions differing from the original design values. The used correlation for the lift cost in € is (after currency conversion from $ to €) as follows:

$$C_{tr} = 425000 \cdot \left\{ 1 + k_T \left(\frac{T_l - T_{l,0}}{T_{l,0}} \right) \right\} \cdot \left\{ 1 + k_m \left(\frac{\dot{m} - \dot{m}_0}{\dot{m}_0} \right) \right\} \cdot \\ \left\{ 1 + k_H \left(\frac{H_l - H_{l,0}}{H_{l,0}} \right) \right\}. \qquad (7)$$

The scaling factors are selected as $k_T = 0.1$ (for temperature dependency), $k_m = 0.65$ (for mass flow dependency), and $k_H = 0.6$ (for lift height dependency). The relevant mass flow is for design point conditions. For the particle lifting, parasitics are calculated considering a 80% efficient vertical lift system. The determined power consumption, which is different for each material, is subtracted from the produced annual electricity.

Ground Particle Transport

For transportation between the solar tower modules and the central power station a number of trucks are foreseen, each transporting insulated containers. To avoid severe thermal cycling of the high temperature containers, one container type is for hot and another type for cold particles, that is, a truck always transports a container set consisting of a hot and a cold container. On the way from an external module to the central module the hot container is charged, and on the way back the cold container is charged. Standard 20 feet ISO containers are assumed for particle ground transport. For such containers a lot of handling equipment is available. The containers are equipped with a 30 cm internal insulation (different type for hot and cold particle containers). With a filling level of 90% an active storage volume of $14.9\,\mathrm{m^3}$ is available per container. The energy content transported by the containers is then defined by the particle mass in this volume and the enthalpy difference between hot and cold particles. With the given temperature difference, the energy content depends on the type of particles used in the system. For a hot particle container, a cost of 90,000 $ is assumed, for a cold particle container 60,000 $, with the difference stemming from the different insulation type according to the temperature level. The cost of a container set is then $C_{containerset} = 150{,}000$ \$.

A truck can serve one or multiple modules, depending on the required mass flow. Mass flow per truck cycle is defined by the container's energy content, the path length, and the loading/ unloading time. The trucks are continuously operated whenever the power cycle is producing electricity, for example, also during night time. As the paths between the solar tower modules and the central power block are clearly defined, fully autonomous trucks are foreseen. Such truck systems are known as automated guided vehicles (AGV); commercial solutions are available. The cost of each truck is assumed as $C_{truck} = 100{,}000$ \$. In addition to the truck and container cost, for each tower a container loading system was accounted for, with cost of $C_{loading} = 50{,}000$ \$ per tower. The number of trucks to provide the required mass flow is calculated from the total path length and the timing conditions. The total ground transport cost is calculated as follows:

$$C_{transport} = C_{truck} \cdot n_{truck} + C_{containerset} \cdot n_{truck} + C_{loading} \cdot n_{mod}. \quad (8)$$

The number of trucks and container sets varies depending on the material properties. Additional thermal losses of 2% are assumed for the particle lifting and ground transportation, reducing the annual yield by this amount. This loss is associated with the thermal losses of the containers and the losses due to filling/emptying procedures. Estimates on the ground transport power consumption showed that this is negligible.

Thermal Storage System

For the solar tower system, a thermal storage time of 12 h full load operation is assumed, resulting in a total thermal storage capacity E_{st} of 3.49 GWh. This storage capacity is evenly distributed over all solar tower modules, leading to a module storage capacity of 249 MWh. The hot and cold storage containments are installed inside the tower, using the tower walls as containment walls. An inner insulation prevents the concrete tower walls from overheating.

Thermal losses in the storage system are assumed as 2% of the total energy provided by the receiver. The total particle inventory per module depends on the selected particle material and is calculated as follows:

$$m_{st} = \frac{E_{st}}{n_{mod} \cdot \Delta h_{total}}. \qquad (9)$$

The total enthalpy difference Δh_{total} is the sum of the reaction enthalpy and the sensible heat between upper and lower temperature of the particles.

For the total particle mass another 5% of this particle mass is added to account for particles contained in components other than the storage, for example, the transportation containers. Mass loss during the plant lifetime is not taken into account here. The cost of the total particle inventory C_{part} is then calculated from the specific particle $C_{sp,part}$ cost as follows:

$$C_{part} = 1.05 \cdot m_{st} \cdot n_{mod} \cdot C_{sp,part}. \qquad (10)$$

The cost of the storage containment C_{stc} is calculated from the surface area A_{stc} of the containment. A cylindrical containment with a height-to-diameter ratio of 1.6 is assumed. From the particle inventory, m_{st}, the volume of the containment is calculated, accounting for a useable filling level of 80%. With the derived diameter and height data the outer surface area is calculated. A temperature-dependent area-specific insulation cost $C_{A,sp,is}$ $[\text{€/m}^2]$ is calculated as follows:

$$C_{A,sp,is}(T_{st}) = 2000 \cdot \left(1 + 0.3 \cdot \frac{(T_{st} - 600)}{400} \right). \qquad (11)$$

The total storage containment cost for all modules is the sum of the cost of the hot and cold storage containments, as given below:

$$C_{stc} = \left\{ A_{stc} \cdot C_{A,sp,is}(T_{r,ex}) + A_{stc} \cdot C_{A,sp,is}(T_{r,in}) \right\} \cdot n_{mod}. \qquad (12)$$

The total cost of the storage system C_{st} is then obtained as the sum of C_{part} and C_{stc}.
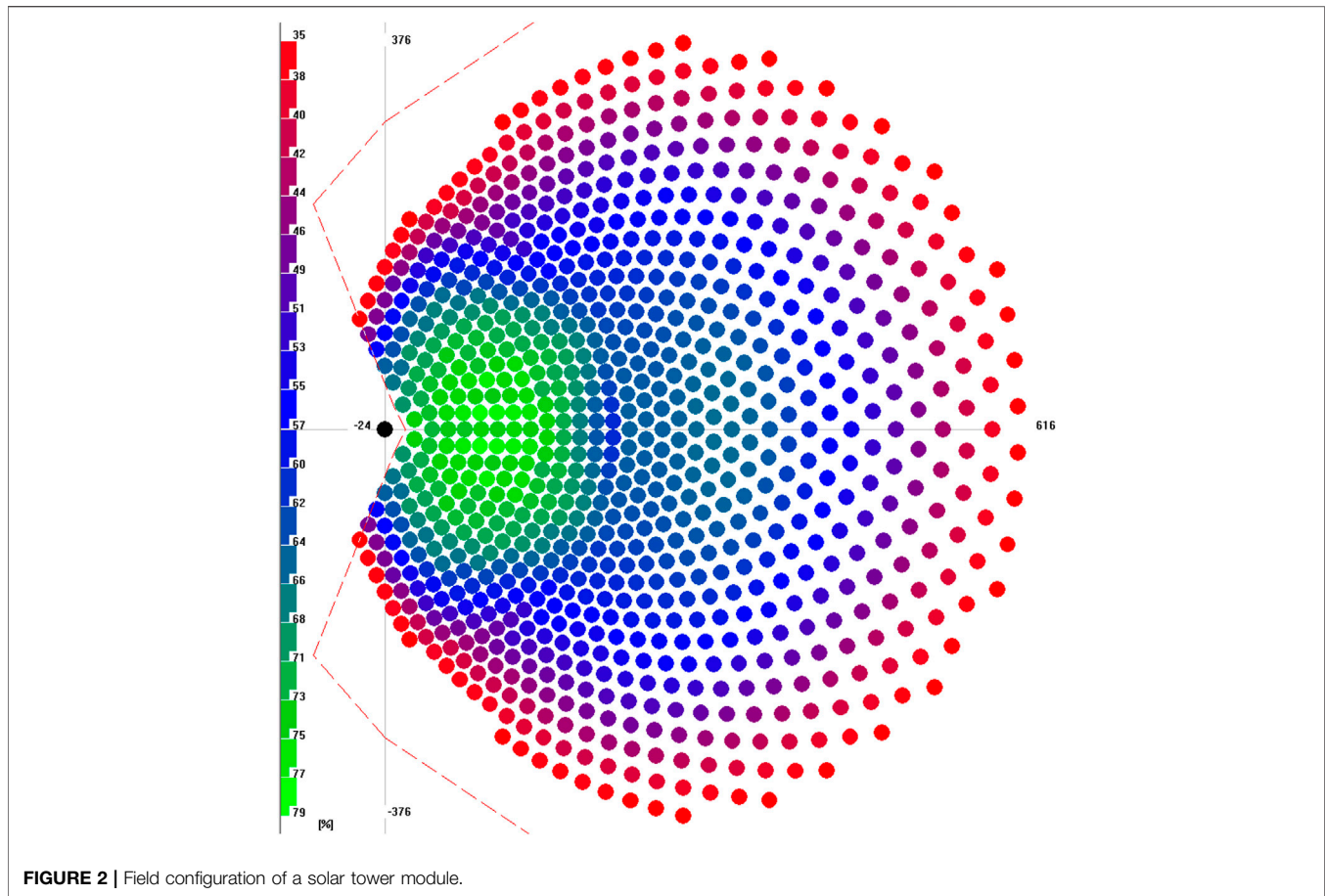
FIGURE 2 | Field configuration of a solar tower module.

LCOE Evaluation

The levelized cost of electricity (LCOE) is selected as the evaluation criteria. The total capital expenditure (CAPEX) is the sum of all module cost plus the cost of the central power block (steam generator and power cycle). Contingencies of 20% are added to the total CAPEX. Annual operational expenditures (OPEX) are assumed as 2% of the CAPEX. The annual electric power production $E_{el,annual}$ is obtained from the HFLCAL layout calculation, based on the annual thermal energy harvested at the selected site. The LCOE is then calculated using a simplified annuity approach as follows:

$$LCOE = \frac{CAPEX\, f_{annuity} + OPEX}{E_{el,annual}}. \qquad (13)$$

The annuity factor $f_{annuity}$ is based on interest rate and the depreciation period. With an interest rate of 7% and a depreciation period of 25a an annuity factor $f_{annuity}$ of 8.58% is obtained. Whenever costs are given in $, they are converted to € with an exchange rate of 1 € = 1.1851 $ (March 09, 2021).

System Layout

For the given fixed temperature range and power requirement, the heliostat field layout and the number of heliostats were optimized using the simulation tool HFLCAL (Schwarzbözl

et al., 2009). A radially staggered field layout is selected. As a result, the field layout, the number of heliostats, and total heliostat field area are obtained together with the tower height and the receiver aperture diameter and the tilt angle. The field, receiver, and tower layout are done for the reference system with bauxite particles, and these components are kept the same for the cases with thermochemically active particles. The resulting field layout for a single module is shown in **Figure 2**. In total 869 heliostats are required to obtain 50 MW$_{th}$ design point power from the receiver. Further layout results are as follows:

- receiver diameter: 5.9 m
- receiver tilt angle (vs. horizontal): 34°
- receiver aperture center height: 111.7 m
- total tower height: 118.7 m (for shadowing calculations)

For the cases with redox materials the following components are adapted:

- storage (variation of size)
- particle inventory (mass)
- heat exchanger (variation of heat exchange area)
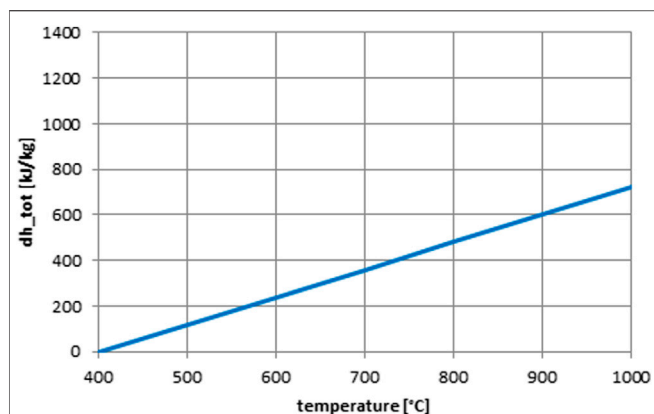- transport system (variation of mass flow)

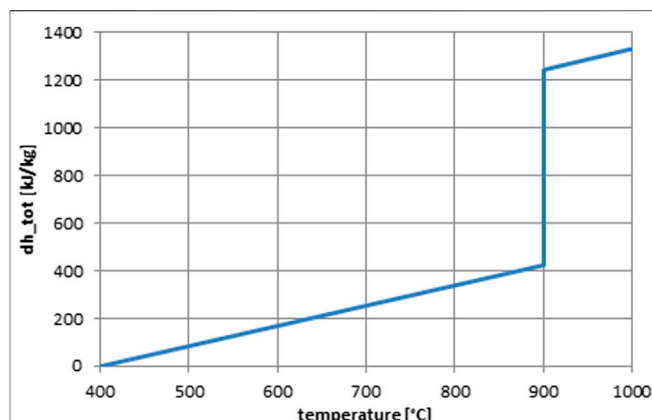**FIGURE 3 |** Enthalpy data for bauxite material (as reference).

FIGURE 4 | Enthalpy data for cobalt-based redox material.

CASE DESCRIPTIONS

The evaluated cases differ by the selected particle material. The following cases are considered:

- bauxite particles (inert particles, reference case)
- cobalt oxide–based redox particles
- manganese/iron oxide–based redox particles
- calcium–manganese–based perovskite redox particles

For the thermochemical particles, the following simplifying assumptions are made:

- chemical reactions are assumed to be not limited by reaction kinetics
- the reaction is proceeding from 0 to 100% within the used temperature range of the particles, and vice versa
- as the thermophysical properties of the redox materials change with the reaction, the values for density and specific heat capacity were approximated by constant average values.
- additional equipment for the reaction process is not considered (e. g. air system for the steam generator)

Since the cost of the selected particles at large quantities is only known for the bauxite material, the comparison between materials is done by the particle break-even cost. This cost is the specific particle cost at which the same LCOE is achieved as in the reference case with bauxite. For each material this break-even cost is determined and discussed.

Bauxite Material

As the reference case, the use of bauxite particles as sensible–only storage medium, as currently proposed by several research teams, is included. Bauxite particles are produced in huge quantities, for example, for use in fracking or casting processes. A heat capacity of $c_{p,part}$ = 1200 J/kgK (Siegel et al., 2014) and a particle bulk density of ρ_{part} = 2000 kg/m³ are assumed. For comparison with the curves for the thermochemical materials, the enthalpy curve for bauxite with the above properties is shown in **Figure 3**. A specific particle cost of $C_{sp,part}$ = 1 \$/kg is assumed, based on quotations for proppants.
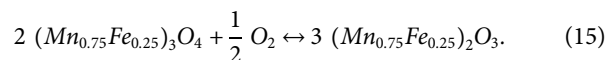
Cobalt-Based Redox Material

For the cobalt-based redox materials, the following reaction is considered:

$$3\,CoO + \frac{1}{2}\,O_2 \leftrightarrow Co_3O_4. \qquad (14)$$
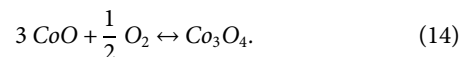
The reaction enthalpy is 844 kJ/kg, and the idealized reaction equilibrium temperature is at 900°C (Block and Schmücker, 2016). **Figure 4** shows the idealized enthalpy curve as function of temperature.

Manganese–Iron–Based Redox Material

For the manganese–based redox materials, the following reaction is considered:

$$2\,(Mn_{0.75}Fe_{0.25})_3O_4 + \frac{1}{2}\,O_2 \leftrightarrow 3\,(Mn_{0.75}Fe_{0.25})_2O_3. \qquad (15)$$

The advantage of this system vs. the pure manganese oxide redox pair Mn_3O_4/Mn_2O_3 examined in our previous work (Buck
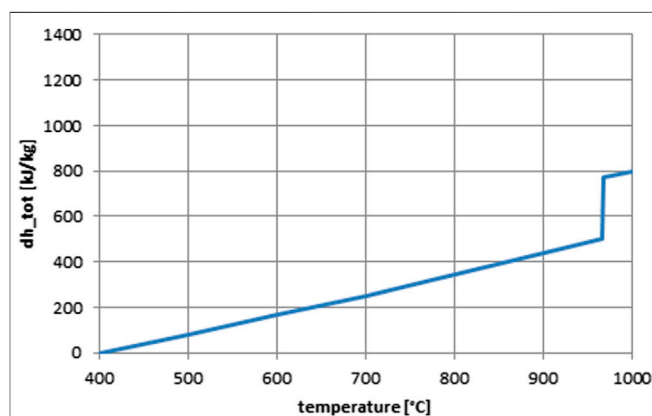

FIGURE 5 | Enthalpy data for manganese–iron–based redox material.

et al., 2020) is that the latter shows a hysteresis between reduction and oxidation, that is, oxidation takes place at about 800°C and reduction happens at about 1,000°C. On the contrary, in the mixed Mn–Fe composition this hysteresis is mitigated (Carrillo et al., 2015), and if the reduced oxide is cooled down slowly enough it can be almost eliminated, so that reduction and oxidation can take place at temperatures very close to each other (Agrafiotis et al., 2015). Hence, a single fixed reaction temperature of 967°C is used in the analysis presented here. The reaction enthalpy of this system is 271 kJ/kg (Preisner et al., 2020). **Figure 5** shows the simplified enthalpy curve as function of temperature used in the system analysis.

Perovskite-Based Redox Material

For the perovskite-based redox materials, the situation is more complex. The Co_3O_4/CoO and $(Mn_{0.75}Fe_{0.25})_3O_4/$ $(Mn_{0.75}Fe_{0.25})_2O_3$ systems considered so far belong to the class of so-called stoichiometric (or phase change) redox oxides (Bulfin et al., 2017a). In such materials, all the cations of the multivalent metal are transformed from the higher to the lower oxidation state during reduction upon heating and vice versa during oxidation upon cooling, at distinct, reduction/oxidation equilibrium temperatures where "abrupt" oxygen release/ uptake takes place in a stoichiometric proportion accompanied by the respective weight loss/gain and endothermal/exothermal effects (**Figures 4**, **5**). On the contrary, perovskites–mixed oxides with multivalent cations of the type ABO_3–belong to the class of the so-called non-stoichiometric (or partial reduction or oxygen vacancy) ones. In the materials of this category, the reduction product does not contain all the reducible metal cations at their lower valence state but only a smaller percentage of them. Oxygen is allowed to move through and leave the lattice through the formation of oxygen vacancies without causing phase transformations that induce crystal structure disruption. Substantial fractions of vacancies can be sustained on the oxide ion sites to enable stoichiometries $ABO_{3-\delta}$. Therefore, such materials react via the following scheme, where the extent of partial reduction δ depends on temperature and oxygen partial pressure and is usually much smaller than 1, as given below:

$$ABO_{3-\delta} + \frac{\delta}{2} O_2 \leftrightarrow ABO_3. \qquad (16)$$
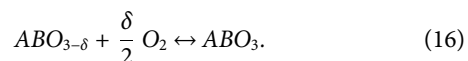
Furthermore, the oxide reduction reaction has an equilibrium partial pressure of oxygen that changes with temperature. Therefore, upon heating under an initial oxygen partial pressure (e.g., 0.21 bar in the case of air at ambient pressure), the reduction of these materials does not take place at a specific distinct equilibrium temperature but within a wide temperature range: as soon as the onset temperature of this reduction is crossed upon heating, the materials release oxygen in a continuous, quasi-linear mode during further heating. The phenomenon is reversible during cooling/oxidation. The extent of reduction/oxidation and the consequent weight change as well as enthalpy effects depend on the particular temperature and partial pressure of oxygen reached. That is exactly the rationale behind performing the reduction of these materials under very

low oxygen partial pressures and their subsequent oxidation under high (oxygen partial) pressures, mentioned in the Introduction section, so that the enthalpy effects recovered during oxidation can be higher than the ones needed during reduction (of course, this scheme has the additional energy penalty of providing the necessary low oxygen partial pressure).

However, in this framework, the reduction/oxidation reaction enthalpies are also absorbed/released in a similar gradual matter with increasing/decreasing temperature. Therefore—unless any other exothermic/endothermic phenomena like for example, relevant to phase transformations take place, which is sometimes the case—the respective enthalpy–temperature plot for these materials will not be characterized by a vertical "step" at the reduction onset temperature like these of the cobalt and manganese–iron oxides in **Figures 4**, **5**, but it should rather be conceived as a continuous "quasi-linear" enhancement of the material's sensible heat capacity that augments the overall amount of energy stored (sensible + thermochemical) beyond this onset temperature (e.g., Albrecht et al., 2016). The magnitude of this "enhancement" as already argued, depends naturally on the material's composition and the actual reduction procedure followed. In this respect, in the quest for materials with higher reducibility, many literature studies follow an approach based on thermodynamic modeling of the extent of reduction δ for a specific material composition as a function of temperature and oxygen partial pressure, complemented by thermogravimetric analysis/differential scanning calorimetry (TGA/DSC) experiments to determine equilibrium values, that either through the van't Hoff (Mastronardo et al., 2020) or through point defects (oxygen vacancies) equilibrium approach (Bulfin et al., 2017b; Albrecht et al., 2018), produce P-T-δ relationships as charts of isothermal or isobaric or "iso-δ" curves. Parametric studies with respect to the kind and the quantity of the dopant elements can then identify optimal material compositions and respective conditions for a given (or maximum possible) reduction extent, δ. Following the relevant work in redox-oxide–based thermochemical water splitting, the first targeted perovskite families were lanthanum manganites, $LaMnO_3$ (LM) doped with strontium, cobalt, and iron (Babiniec et al., 2015). However, more recent studies seem to converge to that calcium manganite; $CaMnO_3$ (CM)-based perovskites are more promising in thermochemical storage applications, on the one hand due to their more suitable thermodynamic properties and on the other hand due to the lower cost and higher earth-abundance of the constituent elements (Bulfin et al., 2017b; Jackson et al., 2019; Babiniec et al., 2016; Babiniec et al., 2020, Mastronardo et al., 2020).

In the vast majority of these thermodynamic studies, even though the temperature range span corresponds to that to be encountered in a solar thermal power tower plant (i.e., from 400–500°C up to 1,100–1,300°C), the respective pressure range usually spans very low oxygen partial pressures (from 0.21 down to 10^{-2} or 10^{-4} atm). Hence, the calculated reduction enthalpies presumably to be recovered through oxidation cited therein, usually correspond to an extent of δ achievable only under very low oxygen partial pressures. The same holds true for many "perovskite
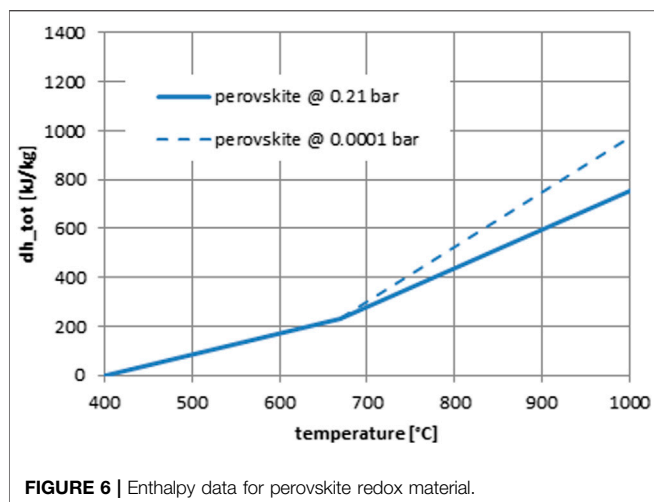
FIGURE 6 | Enthalpy data for perovskite redox material.

materials screening" small-scale experimental studies aimed at quantifying these parameters, that is, weight loss, δ, and reduction enthalpy as a function of operating temperature and oxygen partial pressure, usually through TGA/DSC mentioned above: reduction is performed under reduced oxygen partial pressure, equilibrium is achieved, and then reoxidation is implemented via a stream of much higher oxygen partial pressure.

In our case, for an objective comparison among plants operating under the same boundary conditions, like for example, an open-air particle receiver, data for the reduction of perovskites under ambient air atmosphere has to be employed. For a first comparison among the systems considered in this study, we selected the widely studied for TCS applications material composition $CaMnO_3$ and the very relevant to that doped with a small amount of strontium $Ca_{0.9}Sr_{0.1}MnO_{3-\delta}$. The specific heat capacity of this compound is known and the thermodynamically calculated enthalpy of reduction had the reduction taken place at an oxygen partial pressure of 0.0001 bar and a final temperature of 1,000°C which can be considered as an upper practical limit with today's technology, has been calculated as 455 kJ/kg (Imponenti et al., 2017). Furthermore, the temperature at which the material starts to release oxygen upon heating under air is around 670 °C (Agrafiotis et al., 2019), and a reduction enthalpy under air has been reported as 240 kJ/kg (Yilmaz et al., 2021). Based on this data, **Figure 6** shows the respective enthalpy curves for the two cases, reduction under low oxygen partial pressure and under air, as function of temperature. The fit function for the latter case has been used in the system analysis.

Since the extend of reduction δ, depends on the temperature and partial oxygen pressure, under the conditions considered, that is, reduction temperature of 1,000°C, δ varies between 0.34 and 0.09 for an oxygen partial pressure ranging between 10^{-55} and 1 (as can be read from the isothermal curves on a δ vs. P chart like the ones mentioned above, and in the study by Imponenti et al. (2017). For the particular case selected in the present study for oxidation with air, δ = 0.13.

RESULTS AND DISCUSSION

Table 1 summarizes the relevant properties of the considered materials and the consequences for the storage system. The data is based on the total storage capacity of 3.490 GWh, excess particle material is not included here, only the values for a fully charged storage are given.

The bulk density of the cobalt and perovskite oxide materials was calculated from the pure material density from the study by Jackson et al. (2019) assuming a packing density of 64%.

From the thermophysical data point of view, the cobalt-based material is clearly advantageous. This material leads to significantly reduced storage mass and quite small storage volume. For the manganese–iron–based material, the additional reaction enthalpy is largely offset by the low specific heat capacity and bulk density, so in the end the storage mass is only slightly less than the bauxite reference, and storage volume is even higher. The perovskite material shows about 5% advantage for mass and about 34% advantage for volume, compared to bauxite.

The results of the analysis show that some redox materials can significantly reduce the required storage mass and volume, while others lead only to a marginal improvement. More important than these effects is the impact on LCOE which is affected by the particle cost and other material-dependent cost factors. As no reliable cost information is currently available for mass-produced thermochemically active particles, the particle break-even cost is evaluated for each material.

The system cost consists of fixed and material-dependent contributions. Fixed cost items of the solar power plant are as follows:

- heliostat field: 104.8 M€ (12,166 heliostats)
- tower: 56.35 M€
- receiver: 26.75 M€
- power cycle excl. steam generator: 87.5 M€

Material-dependent contributions are listed in **Table 2**, together with the particle break-even cost to achieve the same LCOE as the reference case.

It should be noted here that a high particle break-even cost is an advantage, meaning that high material cost is allowable while still achieving the same LCOE as the reference system. In consequence, the particle inventory cost can be relatively high in this case since it is based on the high particle break-even cost.

The main findings from the results are as follows:

- for cobalt-based materials: storage mass and storage volume are significantly reduced, as well as the size of the steam generator. This results in reductions in steam generator and the storage containment cost. For breakeven the specific particle cost can be about 6x higher than for bauxite materials, significantly increasing the particle inventory cost. However, it is expected that cobalt-based materials are even more expensive than the break-even cost, making this material unattractive.

TABLE 1 | Comparison of thermophysical properties of considered materials (values from: [a][Jackson et al., 2019], [b][Wokon et al., 2017b], [c][Imponenti et al., 2017], [d][Yilmaz et al., 2021], [e][Preisner et al., 2018]).

		Bauxite	Cobalt	Manganese-iron	Perovskite
Avg. specific heat capacity	[kJ/kgK]	1.2	0.86[a]	0.88[a]	0.86[a]
sensible heat 400–1,000°C	[kJ/kg]	720	516	528	516
Reaction enthalpy	[kJ/kg]	0	844[a]	271[b]	240[d] (P_{O2} = 0.21 bar) 455[c] (P_{O2} = 0.0001 bar)
Total enthalpy difference	[kJ/kg]	779	1,360	799	756 (P_{O2} = 0.21 bar)
Volumetric enthalpy difference	[MJ/m³]	1,558	5,318	1,230	2,192
Ratio R_{tc} (**Eq. 3**)	[-]	1.00	2.64	1.51	1.47
Bulk density	[kg/m³]	2000	3910[a]	1539[b]	2899[a]
storage mass	[t]	17,442	9,234	15,717	16,611
storage volume	[m³]	10,902	2,951	12,765	7,162

TABLE 2 | Cost contributions and the particle break-even cost of considered materials.

		Bauxite	Cobalt	Manganese-iron	Perovskite
LCOE	[€/MWh]	64.9	64.9	64.9	64.9
Total system cost	[M€]	435.5	436.5	435.7	435.6
Steam generator area	[m²]	4,044	1,534	2,672	2,760
Steam generator cost	[M€]	31.9	16.84	24.29	24.82
Particle inventory cost	[M€]	15.45	52.99	19.55	31.35
Particle inventory cost share		3.5%	12.1%	4.5%	7.2%
storage containment cost	[M€]	28.87	12,08	32.07	21.82
specific storage cost	[€/kWh]	12.7	18.7	14.8	15.2
Particle lift cost	[M€]	5.99	4.58	5.70	5.85
Particle ground transport cost	[M€]	5.23	1.86	6.08	3.76
Particle break-even cost	[€/kg]	0.844	5.465	1.184	1.798

- for manganese–iron–based materials: storage volume and total storage cost are increased while steam generator cost is decreased. The particle break-even cost is about 1.4x higher than that for bauxite materials.
- for perovskite materials: storage volume and the storage containment cost are reduced as well as the steam generator cost. The particle inventory cost is increased with the particle break-even cost that is about 2.1x higher than that for bauxite materials.
- changes in the transportation cost have only a minor impact on the system cost and LCOE.

Since several aspects of the redox systems are not well known yet, the analysis is based on several simplifications that need to be validated by future work. The evaluation is considered optimistic for the following reasons:

- reaction kinetics are neglected in the analysis. The effects of reaction kinetics will reduce the benefit from thermochemically active particles in two ways:

  o larger steam generators will be required than assumed in the above analysis, the cost of the steam generator will increase.

  o the reaction extent might be lower than equilibrium conditions

- additional plant equipment required for the reactive system is not considered (air loop, recuperator, and blower); these

components will also introduce additional parasitic power consumption and thermal losses from the hot air stream.

In that sense, the determined particle break-even cost is considered as an indication for particle selection. Only those particle materials that can be mass-produced at cost lower than the break-even cost should be further considered. Using cost assumptions for the raw materials, especially the perovskite materials seem to be promising candidates for future work.

CONCLUSION

In the techno-economic system analysis three candidate redox materials were analyzed for their cost reduction potential: cobalt-based, manganese–iron–based, and perovskite-based oxide materials. These cases were compared to a reference process using inert bauxite particles (sensible-only storage). A solar thermal power plant, consisting of 14 identical solar tower modules with a central power block, with a nominal power of 125 MW$_e$ and a storage capacity of 12 h was considered for the analysis. For each storage material a plant layout was made, taking the specific aspects of the material into account: density, reaction enthalpy, and heat capacity. Simplifying assumptions were made for the impact of temperature stabilization in the heat exchanger, due to the ongoing chemical reaction. For each of the redox material options a particle break-even cost was determined, leading to the same LCOE than with bauxite particles. Cost

factors mainly influenced by the material selection are the storage cost and the steam generator cost. The particle transport system cost has only a minor impact. The results show differences in the characteristics of the materials, with significant reduction on storage size and steam generator cost for example for the cobalt-based particles. However, not all redox materials have advantages regarding storage size, as for example for the manganese–iron–based particles the storage size is even increased due to the combination of thermophysical properties with low specific heat capacity. Regarding the economic potential of the candidate redox materials the perovskite particles seem to have advantages, as they can be in principle produced from inexpensive raw materials. It is therefore recommended to focus future research and development work on this material class.

For the impact of the thermochemically active particles the study uses assumptions that might be too optimistic, for example, neglecting reaction kinetics and the estimated reduction of the heat exchanger area. Detailed heat exchanger design and modeling is required to improve the accuracy of predictions.

DATA AVAILABILITY STATEMENT

The raw data supporting the conclusion of this article will be made available by the authors, without undue reservation.

REFERENCES

Agrafiotis, C., Pein, M., Giasafaki, D., Tescari, S., Roeb, M., and Sattler, C. (2019). Redox Oxides-Based Solar Thermochemistry and its Materialization to Reactor/Heat Exchanger Concepts for Efficient Solar Energy Harvesting, Transformation and Storage. *ASME. J. Sol. Energ. Eng.* 141 (2), 021010. doi:10.1115/1.4042226

Agrafiotis, C., Tescari, S., Roeb, M., Schmücker, M., and Sattler, C. (2015). Exploitation of Thermochemical Cycles Based on Solid Oxide Redox Systems for Thermochemical Storage of Solar Heat. Part 3: Cobalt Oxide Monolithic Porous Structures as Integrated Thermochemical Reactors/heat Exchangers. *Solar Energy* 114, 459–475. doi:10.1016/j.solener.2014.12.037

Albrecht, K. J., Jackson, G. S., and Braun, R. J. (2018). Evaluating Thermodynamic Performance Limits of Thermochemical Energy Storage Subsystems Using Reactive Perovskite Oxide Particles for Concentrating Solar Power. *Solar Energy* 167, 179–193. doi:10.1016/j.solener.2018.03.078

Albrecht, K. J., Jackson, G. S., and Braun, R. J. (2016). Thermodynamically Consistent Modeling of Redox-Stable Perovskite Oxides for Thermochemical Energy Conversion and Storage. *Appl. Energ.* 165, 285–296. doi:10.1016/j.apenergy.2015.11.098

Babiniec, S. M., Ambrosini, A., Coker, E. N., and Miller, J. E. (2020). Redox-active Oxide Materials for thermal Energy Storage. US patent US2020/0048106 A1.

Babiniec, S. M., Coker, E. N., Miller, J. E., and Ambrosini, A. (2015). Investigation of La Sr1−Co M1−O3− (M = Mn, Fe) Perovskite Materials as Thermochemical Energy Storage media. *Solar Energy* 118, 451–459. doi:10.1016/j.solener.2015.05.040

Babiniec, S. M., Miller, J. E., Ambrosini, A., Stechel, E. B., Coker, E. N., Loutzenhiser, P. G., et al. (2016). Considerations for the Design of a High-Temperature Particle Reoxidation Reactor for Extraction of Heat in Thermochemical Energy Storage Systems. Proceedings of the ASME 10th

AUTHOR CONTRIBUTIONS

Conceptualization, RB; methodology, RB; software, RB; validation, RB, material investigation, ST, CA, NN, and MS; writing—original draft preparation, RB, CA; writing—review and editing, ST, NN, CA, and MS; visualization, RB; project administration, ST.

FUNDING

ACKNOWLEDGMENTS

International Conference on Energy Sustainability ES2016, Charlotte, North Carolina, ES2016–59646. June 26–30, 2016. doi:10.1115/es2016-59646

Baumann, T., and Zunft, S. (2014). *Eurotherm Seminar #99–Advances in Thermal Energy Storage* 28. Lleida, Spain. 978 84 697 0467 7. 05.-30.05.2014. Experimental Investigation on a Moving Bed Heat Exchanger Used for Discharge of a Particle-Based TES for CSP.

Block, T., and Schmücker, M. (2016). Metal Oxides for Thermochemical Energy Storage: A Comparison of Several Metal Oxide Systems. *Solar Energy* 126, 195–207. doi:10.1016/j.solener.2015.12.032

Buck, R., and Giuliano, S. (2019). Solar Tower System Temperature Range Optimization for Reduced LCOE. *AIP Conf. Proc.* 2126, 030010. doi:10.1063/1.5117522

Buck, R., Tescari, S., Schmücker, M., Preisner, N., and Agrafiotis, C. (2020). Techno-Economic Analysis of Thermochemical Storage for CSP Systems. *AIP Conf. Proc.* 2303, 200002. doi:10.1063/5.0028904

Bulfin, B., Vieten, J., Agrafiotis, C., Roeb, M., and Sattler, C. (2017a). Applications and Limitations of Two Step Metal Oxide Thermochemical Redox Cycles; a Review. *J. Mater. Chem. A.* 5, 18951–18966. doi:10.1039/c7ta05025a

Bulfin, B., Vieten, J., Starr, D. E., Azarpira, A., Zachäus, C., Hävecker, M., et al. (2017b). Redox Chemistry of CaMnO3 and Ca0.8Sr0.2MnO3 Oxygen Storage Perovskites. *J. Mater. Chem. A.* 5 (17), 7912–7919. doi:10.1039/c7ta00822h

Carrillo, A. J., Serrano, D. P., Pizarro, P., and Coronado, J. M. (2015). Improving the Thermochemical Energy Storage Performance of the Mn2O3/Mn3O4 Redox Couple by the Incorporation of Iron. *ChemSusChem* 8, 1947–1954.

Ebert, M., Amsbeck, L., Jensch, A., Hertel, J., Rheinländer, J., Trebing, D., et al. (2016). Upscaling, Manufacturing and Test of a Centrifugal Particle Receiver. PowerEnergy2016-59252, Proc. ASME Energy Sustainability Conference 26, 30. June 2016, Charlotte, United States.

Ebert, M., Amsbeck, L., Rheinländer, J., Schlögl-Knothe, B., Schmitz, S., Sibum, M., et al. (2019). Operational Experience of a Centrifugal Particle Receiver Prototype. *AIP Conf. Proc.* 2126, 030018. doi:10.1063/1.5117530

Flamant, G., Gauthier, D., Benoit, H., Sans, J.-L., Garcia, R., Boissière, B., et al. (2013). Dense Suspension of Solid Particles as a New Heat Transfer Fluid for Concentrated Solar thermal Plants: On-Sun Proof of Concept. *Chem. Eng. Sci.* 102, 567–576. doi:10.1016/j.ces.2013.08.051

González-Portillo, L. F., Albrecht, K., and Ho, C. K. (2021). Techno-Economic Optimization of CSP Plants with Free-Falling Particle Receivers. *Entropy* 23, 76. doi:10.3390/e23010076

Imponenti, L., Albrecht, K. J., Wands, J. W., Sanders, M. D., and Jackson, G. S. (2017). Thermochemical Energy Storage in Strontium-Doped Calcium Manganites for Concentrating Solar Power Applications. *Solar Energy* 151, 1–13. doi:10.1016/j.solener.2017.05.010

Jackson, G. S., Imponenti, L., Albrecht, K. J., Miller, D. C., and Braun, R. J. (2019). Inert and Reactive Oxide Particles for High-Temperature thermal Energy Capture and Storage for Concentrating Solar Power. *ASME J. Sol. Energ. Eng.* 141 (2), 021016. doi:10.1115/1.4042128

Khare, S., Dell'Amico, M., Knight, C., and McGarry, S. (2013). Selection of Materials for High Temperature Sensible Energy Storage. *Solar Energ. Mater. Solar Cell* 115, 114–122. doi:10.1016/j.solmat.2013.03.009

Ma, Z., Glatzmaier, G. C., and Mehos, M. (2014). Development of Solid Particle thermal Energy Storage for Concentrating Solar Power Plants that Use Fluidized Bed Technology. *Energ. Proced.* 49, 898–907. doi:10.1016/j.egypro.2014.03.097

Mastronardo, E., Qian, X., CoronadoHaile, J. M. S. M., and Haile, S. M. (2020). The Favourable Thermodynamic Properties of Fe-Doped CaMnO3 for Thermochemical Heat Storage. *J. Mater. Chem. A.* 8, 8503–8517. doi:10.1039/d0ta02031a

Matches Equipment Cost (2018). Available at: http://matche.com/equipcost/Exchanger.html (Accessed 06 22, 2018).

Mehos, M., Turchi, C., Vidal, J., Wagner, M., Ma, Z., Ho, C., et al. (2017). Concentrating Solar Power Gen3 Demonstration Roadmap. NREL/TP-5500-67464, 2017.

Miller, J. E., Ambrosini, A., Babiniec, S. M., Coker, E. N., Ho, C. K., Al-Ansary, H., et al. (2016). High Performance Reduction/oxidation Metal Oxides for Thermochemical Energy Storage (PROMOTES) 2016, Proceedings of the ASME 10th International Conference on Energy Sustainability ES2016, Charlotte, North Carolina, ES2016–59660. June 26–30, 2016. doi:10.1115/es2016-59660

Neises, M., Tescari, S., de Oliveira, L., Roeb, M., Sattler, C., and Wong, B. (2012). Solar-heated Rotary kiln for Thermochemical Energy Storage. *Solar Energy* 86, 3040–3048. doi:10.1016/j.solener.2012.07.012

Preisner, N. C., Block, T., Linder, M., and Leion, H. (2018). Stabilizing Particles of Manganese-Iron Oxide with Additives for Thermochemical Energy Storage. *Energy Technol.* 6 (11), 2154–2165. doi:10.1002/ente.201800211

Preisner, N. C., Bürger, I., Wokon, M., and Linder, M. (2020). Numerical Investigations of a Counter-current Moving Bed Reactor for Thermochemical Energy Storage at High Temperatures. *Energies* 13, 772. doi:10.3390/en13030772

Preisner, N. C., and Linder, M. (2020). A Moving Bed Reactor for Thermochemical Energy Storage Based on Metal Oxides. *Energies* 13, 1232. doi:10.3390/en13051232

Repole, K. K. D., and Jeter, S. M. (2016). Design and Analysis of a High Temperature Particulate Hoist for Proposed Particle Heating Concentrator Solar Power Systems. *ASME Energy Sustainability* 2016. doi:10.1115/ES2016-59619

Schöniger, F., Thonig, R., Resch, G., and Lilliestam, J. (2021). Making the Sun Shine at Night: Comparing the Cost of Dispatchable Concentrating Solar Power and Photovoltaics with Storage. *Energ. Sourc. B: Econ. Plann. Pol.* 16 (1), 55–74. doi:10.1080/15567249.2020.1843565

Schrader, A. J., Bush, H. E., Ranjan, D., and Loutzenhiser, P. G. (2020). Aluminum-doped Calcium Manganite Particles for Solar Thermochemical Energy Storage: Reactor Design, Particle Characterization, and Heat and Mass Transfer

Modelling. *Int. J. Heat Mass Transfer* 152, 119461. doi:10.1016/j.ijheatmasstransfer.2020.119461

Schrader, A. J., Muroyama, A. P., and Loutzenhiser, P. G. (2015). Solar Electricity via an Air Brayton Cycle with an Integrated Two-step Thermochemical Cycle for Heat Storage Based on Co3O4/CoO Redox Reactions: Thermodynamic Analysis. *Solar Energy* 118, 485–495. doi:10.1016/j.solener.2015.05.045

Schwarzbözl, P., Pitz-Paal, R., and Schmitz, M. (2009). *Visual HFLCAL–A Software Tool for Layout and Optimisation of Heliostat Fields.* Berlin: Proceedings SolarPACES.

Siegel, N., Gross, M., Ho, C., Phan, T., and Yuan, J. (2014). Physical Properties of Solid Particle thermal Energy Storage media for Concentrating Solar Power Applications. *Energ. Proced.* 49, 1015–1023. doi:10.1016/j.egypro.2014.03.109

Siegel, N. P., Gross, M. D., and Coury, R. (2015). The Development of Direct Absorption and Storage media for Falling Particle Solar central Receivers. *J. Solar Energ. Eng.* 137, 041003. doi:10.1115/1.4030069

Tamme, R., Taut, U., Streuber, C., and Kalfa, H. (1991). Energy Storage Development for Solar thermal Processes. *Solar Energ. Mater.* 24, 386–396. doi:10.1016/0165-1633(91)90077-x

Tescari, S., Singh, A., Agrafiotis, C., de Oliveira, L., Breuer, S., Schlögl-Knothe, B., et al. (2017). Experimental Evaluation of a Pilot-Scale Thermochemical Storage System for a Concentrated Solar Power Plant. *Appl. Energ.* 189, 66–75. doi:10.1016/j.apenergy.2016.12.032

Tescari, S., Sundarraj, P., Moumin, G., Duarte, J. P. R., Agrafiotis, C., de Oliveira, L., et al. (2020). Solar Rotary kiln for Continuous Treatment of Particle Material: Chemical Experiments from Micro to Milli Meter Particle Size. *AIP Conf. Proc.* 2303, 140007. doi:10.1063/5.0029271

Weinrebe, G., von Reeken, F., Wöhrbach, M., Plaz, T., Göcke, V., and Balz, M. (2014). Towards Holistic Power Tower System Optimization. *Energ. Proced.* 49, 1573–1581. doi:10.1016/j.egypro.2014.03.166

Wokon, M., Block, T., Nicolai, S., Linder, M., and Schmücker, M. (2017b). Thermodynamic and Kinetic Investigation of a Technical Grade Manganese-Iron Binary Oxide for Thermochemical Energy Storage. *Solar Energy* 153, 471–485. doi:10.1016/j.solener.2017.05.045

Wokon, M., Kohzer, A., and Linder, M. (2017a). Investigations on Thermochemical Energy Storage Based on Technical Grade Manganese-Iron Oxide in a Lab-Scale Packed Bed Reactor. *Solar Energy* 153, 200–214. doi:10.1016/j.solener.2017.05.034

Wong, B. (2011). *Thermochemical Heat Storage for Concentrated Solar Power.* San Diego, CA: Final Report for the U.S. Department of EnergyU.S.A. Available at: http://www.osti.gov/scitech/biblio/1039304/(Accessed on 03 20, 2021).

Wu, W., Amsbeck, L., Buck, R., Uhlig, R., and Ritz-Paal, R. (2014). Proof of Concept Test of a Centrifugal Particle Receiver. *Energ. Proced.* 49, 560–568. doi:10.1016/j.egypro.2014.03.060

Yilmaz, D., Darwish, E., and Leion, H. (2021). Utilization of Promising Calcium Manganite Oxygen Carriers for Potential Thermochemical Energy Storage Application. *Ind. Eng. Chem. Res.* 60, 1250–1258. doi:10.1021/acs.iecr.0c05182

Zunft, S., Hänel, M., Krüger, M., and Dreißigacker, V. (2014). A Design Study for Regenerator-type Heat Storage in Solar Tower Plants-Results and Conclusions of the HOTSPOT Project. *Energ. Proced.* 49, 1088–1096. doi:10.1016/j.egypro.2014.03.118